A Novel Instrument for Real-Time Measurement of Attenuation of Weather Radar Radome Including Its Outer Surface. Part I: The Concept

ALESSIO MANCINI, JORGE L. SALAZAR, RODRIGO M. LEBRÓN, AND BOON LENG CHEONG

School of Electrical and Computer Engineering, and Advanced Radar Research Center, University of Oklahoma, Norman, Oklahoma

(Manuscript received 10 May 2017, in final form 19 December 2017)

ABSTRACT

This paper presents a unique instrument for characterizing the impact of wet radomes in radar systems. The proposed technique enables full radio frequency (RF) characterization of the radome, by evaluating its performance under a variety of conditions, including dirtiness, wetness, ice formation, and varying temperature, and providing a potential solution for future wet radome calibration methods. The reflections generated from the wet radome surface, measured from a high-resolution probe, are combined with an estimation of water absorption as a function of the precipitation rain rate, to calculate the attenuation introduced by the wet radome. This instrument is a cost-effective solution that can be integrated into an existing or new radar system.

1. Introduction

With the introduction of dual-polarization systems in operational radar networks, target accuracy for differential reflectivity Z_{DR} and horizontal reflectivity factor Z_h is required (Zrnić and Doviak 2005; Wang and Chandrasekar 2006). To achieve this goal, all sources of bias must be taken into account, with the primary source of bias being the radome. Agents such as pollution and time degradation deteriorate the hydrophobic property of the radome skin, decreasing the radome performance, especially in the presence of water (Blevis 1965; Anderson 1975; Hendrix et al. 1989; Chang 1985; Fenn 1997). Mitigation of the adverse effect of the wet radome can be accomplished by introducing a hydrophobic or superhydrophobic material to the external radome skin to minimize the impact of a continuous water film over the surface, significantly improving radar performance. Some researchers have taken into account the effect introduced by water on the radome by performing studies in which water was considered as a film (Blevis 1965; Ruze 1965; Chang 1985). Water does not always distribute as a film but also as droplets and rivulets. The impact on the radome of artificial rain was studied by Hendrix et al. (1989) and Fenn (1997) at 20 GHz; Kurri and Huuskonen (2008) at C band and the impact of natural rain was investigated by Anderson (1975) at 20 GHz; Frech (2009) and Frech et al. (2013) at C band; and Frasier et al. (2013) at X band. Thompson and Illingworth (2012) presented a technique to measure the total attenuation from the radome. They showed that old radomes can produce 2–3 dB of attenuation when the rain rate is 2–3 mm h^{-1}. An analytical model to estimate the performance of the wet radome, for a dual-polarized radars operating at X band, was proposed by Salazar-Cerreno et al. (2014). Salazar-Cerreno et al.'s approach found good agreement with experimental data from the Weather Surveillance Radar-1988 Doppler (WSR-88D) and the Center for Collaborative Adaptive Sensing of the Atmosphere (CASA) radar. Díaz et al. (2015) investigated the attenuation of wet X-band radomes for various hydrophobic surfaces as a function of the rain rate. The model created by Díaz et al. was validated through experimental results.

Manz et al. (1999) performed a study evaluating the effects caused by the distribution of joints in the radome on radar performance at C band. Manz et al.'s work suggests the installation of a device to test the transmitted signal and to measure the changes in radome attenuation as a possible solution for wet radome calibration. Bechini et al. (2010) proposed a technique to measure the attenuation under wet conditions for X-band radars. Bechini et al.'s correction based on the disdrometer assumes that water is a film and did not account for rivulet effects that could produce various

Corresponding author: Alessio Mancini, amancini@ou.edu

DOI: 10.1175/JTECH-D-17-0083.1

levels of attenuation in the horizontal (H) and vertical (V) planes. Gorgucci et al. (2013) developed two methods for Z_{DR} calibration, sun and weather target calibrations. Both of the techniques proposed by Gorgucci et al. were validated through experiments. Another study on the effect of wet X-band radomes on radar performance was done by Schneebeli et al. (2012). Schneebeli et al. employed a self-consistent algorithm to estimate the reflectivity offset introduced by the presence of the radome. Using the extended Kalman filter (EKF) algorithm and a standard rain attenuation correction scheme (ZPHI), Schneebeli et al. corrected the X-band radar measurement for both attenuation and differential attenuation. An alternative method was implemented by Frasier et al. (2013) that uses two radars to look at the same volume target. By noticing an increase of reflectivity occurring in only one of the radars, the attenuation resulting from the wetting of the related radome is deduced. The technique proposed by Frasier et al. allows for absolute calibration of radar to be achieved. A possible limitation of using two radars is that the different scan patterns produce a temporal mismatch that results in additional scatter. Furthermore, two radars are not always available to look at the same volume target.

This paper presents a novel technique that enables radio frequency (RF) characterization of any type of radome under any condition. The proposed instrument is a low-cost, low-size solution, and it can be installed in an existing operative radar without significantly affecting the radar signal. One of the novel aspects introduced by the proposed concept is that the radome characterization is based on the reflection coefficient measurement. The new instrument is composed of a reflectometer, time domain gating (TDG) analysis, and a probe. The reflectometer was employed in this research to measure reflections generated at the air–radome interface. The TDG analysis (implemented in the reflectometer) was utilized to remove unwanted reflections coming from the surrounding environment. A suitably designed dielectric rod antenna was employed as a probe. With this instrument it is possible to perform real-time measurement of the reflections because of the radome and water formation on its outer surface and, indirectly, to estimate the transmission loss occurring as a result of the wet radome. The radome is characterized by high-resolution measurements dictated by the probe's beamwidth. High spatial resolution allows for effects introduced by raindrops accumulated on the surface, the impact of scatterer points caused by imperfections that may be present, and the influence introduced by structural joints to be taken into account. Because a narrow-beam probe is employed, the area of the radome analyzed does not match with the area sampled by the parabolic reflector; a trade-off is discussed later in section 4.

Based on the physical conditions of the outer skin of the radome, different water formations are possible. The possible water distributions are droplets and rivulets or a continuous film. Rivulets, given their vertical geometry, are particularly critical because they produce a higher level of reflection in the vertical than the horizontal plane. When a layer of water is formed on the outer surface of the radome, either as droplets or as a continuous film, part of the incident energy is absorbed by the water. To include the water absorption, the method described here calculates the absorptance of water, as a function of the rain rate, without considering the radome. Then, combining the absorption with the reflectance directly measured, it is possible to estimate transmittance through the wet radome. Since the radome stackup is normally unknown, it is not possible to estimate the related absorptance. However, the energy absorbed by a dry radome is normally very small and can be neglected.

To validate the proposed approach, a laboratory setup was designed to measure the reflectance generated from radome panels at X band.

The paper is organized with an explanation of the proposed technique in section 2. The concept and theory, as well as the algorithm to estimate the water absorption, is provided in section 3. In section 4 the setup, the key tools employed for the proposed instrument, and the TDG principles are introduced. The experimental results obtained from the setup are presented and discussed in section 5. The algorithm to estimate the water absorption will be employed in the second part of this paper (Mancini et al. 2018, hereinafter Part II), where additional experiments for the radome characterization are discussed.

2. Proposed measurement system

a. Two-port system

The system commonly used to measure the attenuation introduced by the radome is shown in Fig. 1a. For this configuration, a probe to transmit and a probe to receive are required. The sample material must be placed exactly midway between the antennas, and the probes must be perfectly aligned facing each other. In such a scenario, the incident electromagnetic field is decomposed into reflected and transmitted fields. This mechanism is schematically shown in Fig. 2. This same process happens inside the radome at the radome–air interface, and it occurs infinite times inside the material. The phenomenon described is shown only three times in Fig. 2 to simplify the diagram. The method represented in Fig. 1a was implemented by Díaz et al. (2015).

The limitations of the two-port system in characterizing radomes were discussed in Mancini et al. (2017).

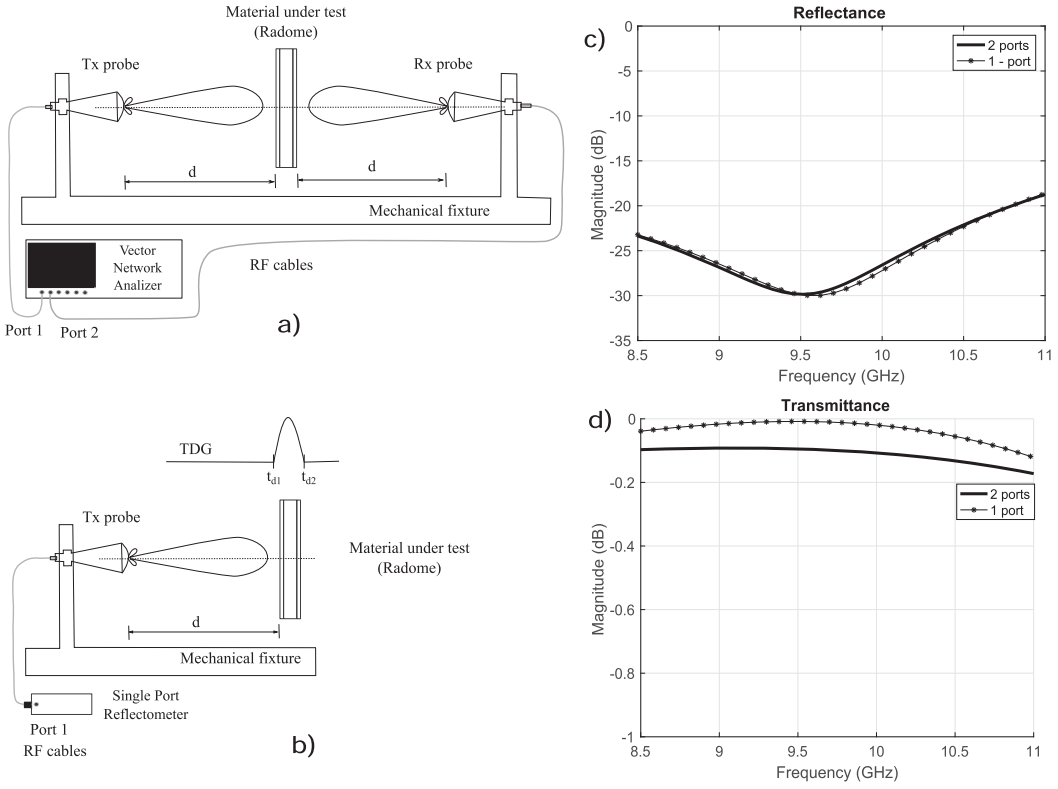

FIG. 1. A schematic representation of the system to characterize radomes for (a) the free-space transmission coefficient technique conventionally used and (b) the new technique using only one probe. The labels in (a) and (b) indicate the probes and the distance d between the antennas and the material under test (radome). The start and stop times of the TDG (t_{d1} and t_{d2}, respectively) are shown in (b). Numerical simulations for the (c) reflection and (d) transmission coefficients are shown for a dry radome. The radome stackup is described in Table 3, below.

b. *One-port system*

The proposed instrument to measure the reflections generated at the air–radome boundary is schematically shown in Fig. 3. A dielectric rod antenna was employed as a probe. The single-port reflectometer, set in a time domain, reads the reflections directly measured by the probe. By mounting the probe at the antenna feed position, scans in azimuth and elevation with the resolution dictated by the radar system are possible. This configuration allows for full real-time RF characterization of the radome. A probe smaller than the antenna feed is required to minimize attenuation caused by a potential blockage. This requirement is necessary in order to measure the radome reflections without affecting the radar performance. A customized probe with a small transversal area and a narrow beam for high-spatial-resolution tests is required. The probe collects reflections generated from the radome in the same direction that the radar is scanning, because it is mounted in the radar antenna. Although mounted on the radar antenna, the operation principle of the radome characterization device is totally independent of the radar, and it does not affect the radar operating bandwidth. The proposed method allows for measuring the effect of water on the radome outer surface when rain reaches the radar location. Water accumulation is not the same on all the parts of the radome. Multiple factors, including dirt on or damage to the radome and blowing wind, can in fact influence water distribution on the surface.

The probe is connected to the single-port reflectometer, and the TDG is set to measure the reflectance at the radome interface, filtering out all the multiple reflections coming from the surrounding environment (section 4). The small-sized instrument, composed of a probe and a reflectometer, allows for ease of transport for infield measurements in the case of mobile radar stations and quick implant in existing operational radars. To simultaneously measure the reflections generated from the radome in the H and V planes, a dual-polarized probe can be suitably designed or two linearly polarized probes, where one is rotated 90° with respect to the other one, can be used. The influence of a dual-polarized probe on the performance of a parabolic reflector antenna was estimated through simulations in Ansys High-Frequency Structural Simulator (HFSS), version 2016. The Ansys

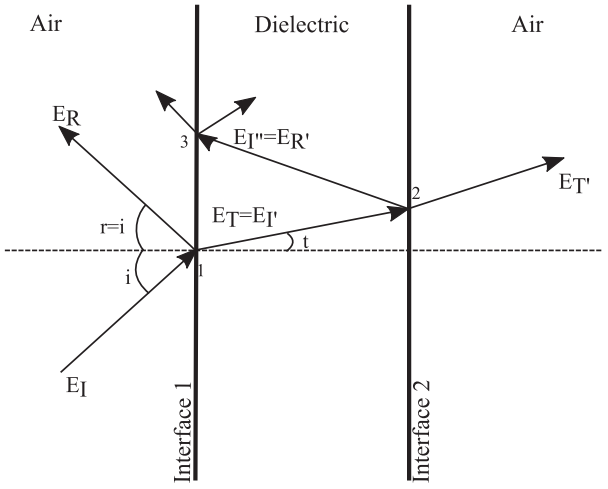

FIG. 2. A dielectric slab separating two media made of air. The sketch shows angular incidence in order to make the representation easier. Shown in the illustration are the angles of incidence, reflection, and transmission (labeled i, r, and t), as well as the incident, reflected, and transmitted electric fields ($\mathbf{E}_I$, $\mathbf{E}_R$, and $\mathbf{E}_T$) at the first interface. Also shown is the transmitted field through the second interface ($\mathbf{E}_{T'}$). The figure shows the multiple reflections occurring inside the slab. To avoid complicating the illustration, this mechanism is shown only three times, once at each interface.

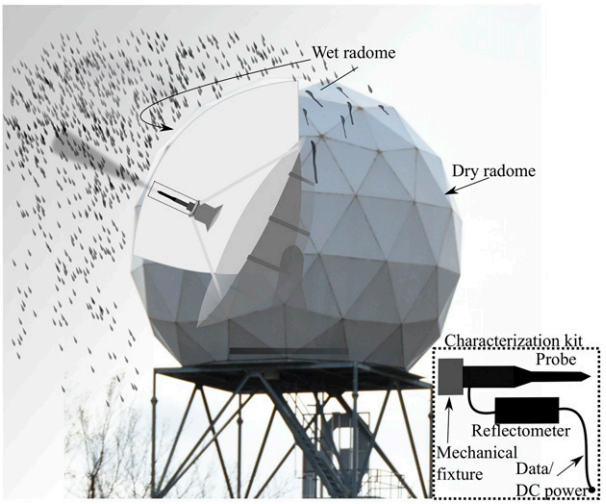

FIG. 3. A schematic representation of the proposed concept, and a detailed illustration of the radome characterization kit.

HFSS software utilizes a 3D, full-wave, frequency domain electromagnetic field solver based on the finite element method. To evaluate the impact of the instrument on an operational radar, two scenarios were considered. The first case simulated the reflector system of the PX-1000 weather radar (Cheong et al. 2013) with no radome included and without the dielectric probes. Two dielectric antennas were then added for a second simulation, placed right behind the feed of the reflector system, to evaluate their effect on the radiation pattern. An illustration and a photograph of the PX-1000 parabolic reflector are shown in Fig. 4. The measured performance of the PX-1000 radar was executed in an outdoor far-field test range by the manufacturer. Unfortunately, a copy of these measurements is not available, but information such as gain, beamwidth, and the levels of sidelobes are provided. A comparison between the measured and simulated performances of the parabolic reflector, without the probes, is presented in Table 1. The gain and beamwidth achieved through simulation are the same as those measured in actual performance, but in the simulation, a lower sidelobe level (SLL) is obtained. The discrepancy between the measured and simulated sidelobe level is probably due to the fact that, since the measurement was done outdoors, multiple reflections have raised the level of the sidelobe, while this does not occur in the simulation. Since the model well represents the actual radar antenna, in terms of both physical dimensions and electrical performance, the effect of the probes can be now evaluated. The results regarding the influence of the dual-polarized probe on the parabolic reflector performance were presented in Mancini et al. (2017) and are summarized in Table 2. Simulations show that the gain is not affected by the presence of the probe, while a rise of the secondary beams is noticeable. The level of the cross polarization, in the range from −5° to 5°, remains the same (Mancini et al. 2017), but the integrated cross polarization, computed for each of the main cuts in azimuth, increases because of the probe's presence. The H plane is the most affected by the presence of the dual-polarized probe. This is probably because the dielectric antennas are aligned in the corresponding direction, presenting a bigger obstruction than in the E plane. Although the impact on the radar performance was evaluated by using a dual-polarized probe, while in the experiments a single-polarized probe was employed, this result is important for validating the technique proposed. Furthermore, by using two probes instead than one, it creates a worst-case scenario with respect to the case where only a single probe was used. Considering the impact of the probe on the radiation pattern of the parabolic reflector, a miniaturized version of the dielectric antenna will be necessary for real-time applications, in order to further reduce its impact on the radar performance.

The probe does not need to sample the radome every time the radar transmits/receives. It is sufficient to take a sample every N times the radar samples. If, for instance, the radar samples N times consecutively, at the $N + 1$ transmitting period, then the probe samples instead of the radar. The echoes from the radar would be very low

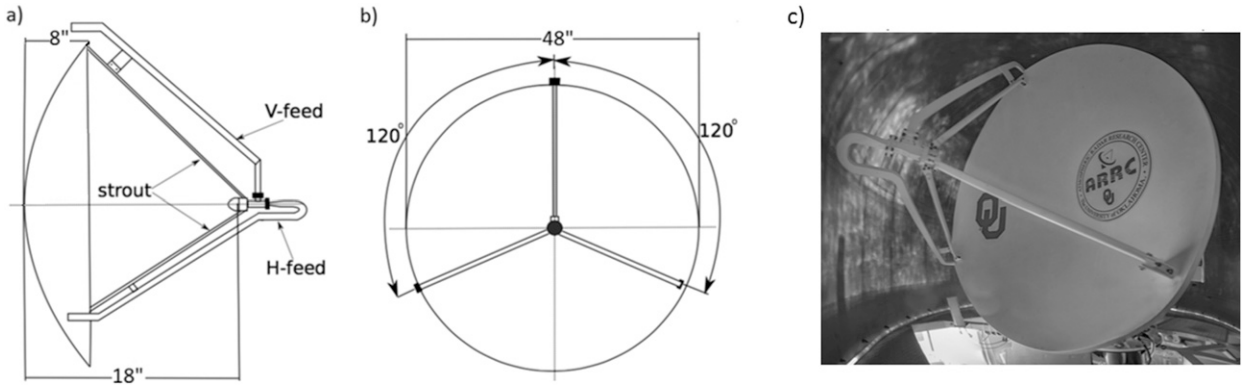

FIG. 4. An illustration of the PX-1000 antenna showing the feed and the struts arrangement, the focal distance (18 in.; 1 in. = 2.54 cm), and the diameter of the parabolic reflector (48 in.). (a) The side view. (b) The front view showing the struts only. (c) A photograph of the parabolic reflector (the photograph was taken by Arturo Yoshiyuki Umeyama).

in this circumstance, and they would not interfere with the probe. Sacrificing one sample every N samples of the radar would not affect the weather measurement. In practice N is about 100. In this way the probe can sample at the same frequency the radar operates without interference from the radar. To relate the data collected to the actual position, synchronization will be required. In this way it is possible to have information about the radome conditions at the same time and in the same position where the radar is scanning.

3. Concept and theory

The presence of water on the radome introduces additional attenuation of the signal. This attenuation occurs through both reflection and absorption, and it depends on the frequency of the signal, as well as the temperature and thickness of the water slab. To quantify the level of signal absorbed by a water film, a mathematical model was created and validated through simulation using Ansys HFSS (version 2016). A complete description of the problem includes starting with the definition of the dielectric constant of a lossy medium (water), then calculating the transmittance through a slab of water for different thicknesses. The complex dielectric constant ε_c for a lossy medium is defined as

$$\varepsilon_c = \varepsilon - j\frac{\sigma}{\omega}. \tag{1}$$

The second term in Eq. (1) represents the losses associated with the conductivity σ. The relative dielectric constant is expressed by

$$\varepsilon_r = \frac{\varepsilon_c}{\varepsilon_0} = \frac{\varepsilon}{\varepsilon_0} - j\frac{\sigma}{\omega\varepsilon_0} = \varepsilon' - j\varepsilon''. \tag{2}$$

From Zhang (2016, 34–37) the real and imaginary parts of ε_r can be expressed as

$$\varepsilon' = \varepsilon_\infty + \frac{(\varepsilon_s - \varepsilon_\infty)[1 + (\lambda_s/\lambda)^{1-\nu}\sin(\nu\pi/2)]}{1 + 2(\lambda_s/\lambda)^{1-\nu}\sin(\nu\pi/2) + (\lambda_s/\lambda)^{2(1-\nu)}} \quad \text{and}$$

$$\varepsilon'' = \frac{(\varepsilon_s - \varepsilon_\infty)(\lambda_s/\lambda)^{1-\nu}\cos(\nu\pi/2)}{1+2(\lambda_s/\lambda)^{1-\nu}\sin(\nu\pi/2)+(\lambda_s/\lambda)^{2(1-\nu)}} + \frac{\sigma\lambda}{2\pi c\varepsilon_0}. \tag{3}$$

The formulas in Eq. (3) are the Debye equations with the modifications introduced by Cole and Cole (1941) to account for spread effects. The term ε_∞ is the high-frequency dielectric constant, ε_s is the static dielectric constant, λ_s is the relaxation wavelength, and ν is the spread parameter. These quantities are dependent on the temperature and can be expressed as (Zhang 2016, 34–37)

$$\varepsilon_s = 78.54[1 - 4.579\times10^{-3}(t-25) + 1.19\times10^{-5}(t-25)^2 - 2.8\times10^{-8}(t-25)^3],$$

$$\varepsilon_\infty = 5.271\,37 + 0.021\,647\,4t - 0.001\,311\,98t^2,$$

$$\nu = -\frac{16.8129}{t+273} + 0.060\,926\,5, \quad \text{and}$$

$$\lambda_s = 0.000\,338\,36\, e^{2513.98/(t+273)}. \tag{4}$$

In Eq. (4) the temperature t is expressed in degrees Celsius. The tangent loss is a parameter that quantifies

TABLE 1. A comparison between the measured and simulated antenna performance of the PX-1000 at 9.55 GHz.

Parameter	Measured	Simulated
Gain (dB)	39.3	39.7
Beamwidth (°)	1.8	1.8
SLL (dB)	−26	−34.6

TABLE 2. Effect of the dual-polarized probe on the performance of the PX-1000 parabolic reflector. The comparison is based on simulation.

Parameter	H plane		E plane		D plane	
	Without probe	With probe	Without probe	With probe	Without probe	With probe
Peak gain (dB)	39.71	39.56	39.71	39.56	39.71	39.56
Sidelobe level (dB)	−36	−32	−36	−29	−33	−31
Integrated cross polarization (dB)	−77.57	−83.12	−78.63	−79.13	−106.13	−103.95

the dissipation of electromagnetic energy occurring inside a lossy material. It refers to the phasor in the complex plane whose real and imaginary components are the resistive and lossy part and the reactive and lossless part, respectively. It is defined by the following relation (Pozar 2012, 9–11):

$$\tan\delta = \frac{\omega\varepsilon'' + \sigma}{\omega\varepsilon'}, \tag{5}$$

where ε_r and $\tan\delta$ of freshwater were computed using Eqs. (4), (3), and (5) for $\sigma = 1.1117 \times 10^{-4}\ \mathrm{S\,m^{-1}}$, and they are plotted for different temperatures in Fig. 5. In the figure, ε_r and $\tan\delta$ are computed from 2 to 11 GHz to compare the electromagnetic performance of water at S and X bands.

Considering a plane wave propagating in a lossy medium, the propagation constant can be written as

$$\gamma = \alpha + i\beta = \frac{\omega N}{c}, \tag{6}$$

where c is the speed of light in the vacuum, and N is the complex refraction index of the medium defined by the following equation:

$$N = \sqrt{\frac{\varepsilon\mu}{\varepsilon_0\mu_0}} = n + ik. \tag{7}$$

The power of such a wave propagating in the z direction is defined by the Poynting vector:

$$\mathbf{S} = \frac{1}{2}\mathrm{Re}(\mathbf{E} \times \mathbf{H}^*). \tag{8}$$

The magnitude of $\mathbf{S}$ is called irradiance I. If the medium is lossy (as is the case of water), part of the energy is absorbed by the material and the irradiance is then attenuated by the following law (Bohren and Huffman 1983, 29–41):

$$I = I_0\, e^{-\alpha z}. \tag{9}$$

The quantity α determines the amount of energy lost by absorption inside the material. The absorption coefficient is defined as

$$\alpha = \frac{4\pi k}{\lambda}. \tag{10}$$

The imaginary part of the refraction index [k in Eq. (7)] determines the rate at which the electromagnetic energy is lost by the material absorption. Considering a plane wave propagating in two semi-infinite media, where the first one is nonabsorbing (air) with a refraction index N_1 and the second material is absorbing with a refractive index $N_2 = n_2 + ik_2$; part of the wave is reflected and

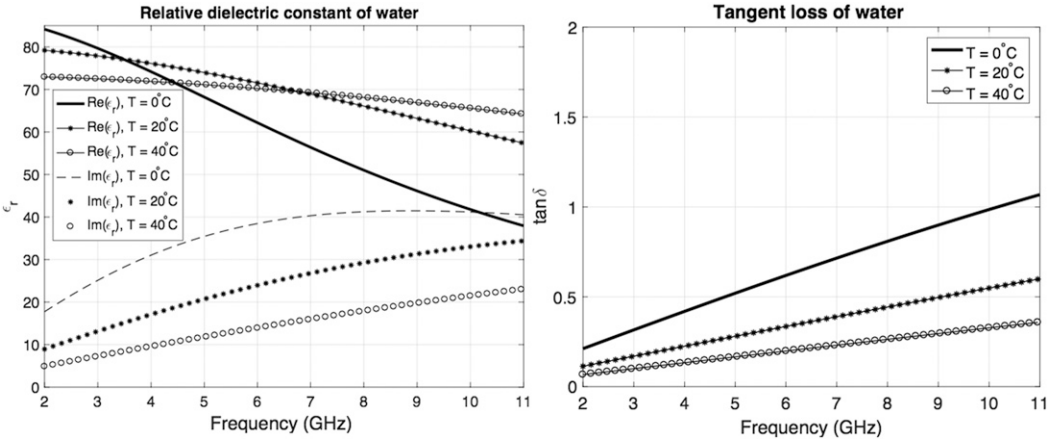

FIG. 5. The dielectric parameters of water for different temperatures: (left) the real and imaginary parts of the relative dielectric constant and (right) the tangent loss.

part is transmitted through the interface. The incident, reflected, and transmitted electric fields are named $\mathbf{E}_I$, $\mathbf{E}_R$, and $\mathbf{E}_T$ respectively. The reflection (r) and transmission (t) coefficients determine the amount of electric field reflected and transmitted, respectively. Such coefficients are defined as

$$r = \frac{|\mathbf{E}_R|}{|\mathbf{E}_I|} \quad \text{and} \quad t = \frac{|\mathbf{E}_T|}{|\mathbf{E}_I|}. \tag{11}$$

Defining the ratio $N_1/N_2 = m$, the coefficients introduced above can be rewritten as (Bohren and Huffman 1983, 29–41)

$$\tilde{r} = \frac{1-m}{1+m} \quad \text{and} \quad \tilde{t} = \frac{2}{1+m}. \tag{12}$$

The reflectance R and the reflection coefficient (as well as the transmittance T and the transmission coefficient) are directly related:

$$R = |\tilde{r}|^2 = \left|\frac{1-m}{1+m}\right|^2 \quad \text{and} \quad T = |\tilde{t}|^2 = \left|\frac{2}{1+m}\right|^2. \tag{13}$$

Considering an absorbing dielectric slab (medium 2, water) of thickness h and refraction index $N_2 = n_2 + ik_2$, placed in between two semi-infinite media made of air, both with $N_1 = n_1$, the folded voltage and power transmission and reflection coefficients t_{slab}, T_{slab}, r_{slab}, R_{slab} at the air–water interface are (Bohren and Huffman 1983, 29–41)

$$\begin{aligned} r_{\text{slab}} &= \frac{\tilde{r}(1 - e^{i2kN_2h})}{1 - \tilde{r}^2 e^{i2kN_2h}}, \\ R_{\text{slab}} &= |r_{\text{slab}}|^2, \\ t_{\text{slab}} &= \frac{4m}{(m+1)^2} \frac{e^{-ikN_1h}}{(e^{-ikN_2h} - \tilde{r}^2 e^{ikN_2h})}, \quad \text{and} \end{aligned} \tag{14}$$

$$T_{\text{slab}} = |t_{\text{slab}}|^2 = \frac{(1-R)^2 + 4R\sin^2\psi}{R^2 e^{-\alpha h} + e^{\alpha h} - 2R\cos(\xi + 2\psi)}, \tag{15}$$

where

$$\psi = \tan^{-1}\left(\frac{2n_1k_2}{n_2^2 + k_2^2 - n_1^2}\right), \quad 0 \le \psi \le \pi, \quad \xi = \frac{4\pi n_2 h}{\lambda}; \tag{16}$$

α was already introduced in Eq. (10), and for this specific case, k needs to be replaced with k_2. The parameter k without subscription, in Eqs. (14) and (15), is the wavenumber ($2\pi/\lambda$). A portion of the electromagnetic wave is transmitted through the first boundary. When it reaches the second interface, it is then partially reflected back to the first boundary and partially transmitted through the second boundary of the slab. This mechanism happens inside the slab infinite times, generating infinite terms that produce the total (folded) reflected or transmitted energy, or equivalently the folded reflectance or transmittance. A sketch of this scenario is presented in Fig. 2 for an angular incidence of the electric field. In the figure the transmitted field is incident ($\mathbf{E}_{I'}$) to the second interface, which reflects part of the field that is incident to the first interface repeatedly ($\mathbf{E}_{I''} = \mathbf{E}_{R'}$). The total transmitted irradiance is written as (Bohren and Huffman 1983, 29–41)

$$I_t = I_i(1-R)^2 e^{-\alpha h}(1 + R^2 e^{-2\alpha h} + R^4 e^{-4\alpha h} + \cdots). \tag{17}$$

The infinite series can be written as

$$T_{\text{slab}} = \frac{(1-R)^2 e^{-\alpha h}}{1 - R^2 e^{-2\alpha h}}. \tag{18}$$

Equation (18) is an approximation of Eq. (15) when the absorption (αh) is large. In this case the oscillatory terms [$\sin^2\psi$ and $\cos(\xi + 2\psi)$] are small relative to the exponential term, and they can be ignored (Bohren and Huffman 1983, 29–41). The same discussion applies to the reflectance.

In the case of a plane wave incident to a boundary separating two lossless media, the law of energy conservation can be written in terms of transmittance and reflectance, as (Balanis 2012, 173–205)

$$T + R = 1. \tag{19}$$

In the scenario where losses occur (absorbing material), Eq. (19) must be rewritten, taking into account the absorptance A of the lossy material (Wallace and Hobbs 1977, 295–296; Antonets et al. 2008):

$$T + R + A = 1. \tag{20}$$

In Eqs. (19) and (20), R and T are the folded reflectance and transmittance for the case of a slab or multilayer material, respectively.

To prove the model assumptions, simulations in Ansys HFSS were performed to represent the concept shown in Fig. 1b. To achieve this goal, two scenarios were replicated, both employing a dry, multilayer radome operating at X band. The first scenario used two ports to emulate the system shown in Fig. 1a. A second simulation to reproduce the scenario in Fig. 1b used one port to excite the incident wave and set the second port as impedance boundary to simulate the free space. Results are presented in Fig. 1c for the reflection coefficient and Fig. 1d for the transmission coefficient. The curves in Fig. 1c are the results of direct simulation. The

TABLE 3. The radome stackup employed in the HFSS simulations to prove the concept shown in Fig. 1. The radome is designed to operate at 9.55 GHz.

Material	Thickness (mm)	ε_r	tanδ
Paint	0.127	3.65	0.035
E-glass epoxy (outer skin)	0.508	4.2	0.017
Nomex (core)	6.8	1.1	0.003
E-glass epoxy (inner skin)	0.508	4.2	0.017

transmission coefficient for the two-port case (thick solid curve in Fig. 1d) is also produced from direct simulation. The curve computed for one port in Fig. 1d is obtained by applying Eq. (19), because the materials considered are low loss. Simulations show good agreement between the two-port and one-port scenarios for both transmission and reflection coefficients, confirming the validity of the approach chosen and assuring that the absorption can be neglected in the case of a dry radome. The absorption for the scenario presented can be evaluated by computing the difference between the two curves in Fig. 1d, which is lower than 0.1 dB. The stackup employed for the X-band radome simulated in HFSS is summarized in Table 3.

To evaluate the impact of the absorption of a slab of water without the radome, an analytical approach considering water at 20°C, with thicknesses of 0.2, 0.6, and 1 mm, was taken into account. First, ε_s and ε_∞ were computed for the selected temperature from Eq. (4), then ε' and ε'', and tanδ were obtained from Eqs. (3) and (5), respectively (Fig. 5 for $T = 20$°C). Then the reflectance and transmittance through the slab were calculated using Eqs. (14) and (15), respectively. The same scenario was replicated in Ansys HFSS. The defined dielectric properties (ε' and tanδ) of the water in the simulator were set to be frequency dependent, as in Fig. 5, in order to assure more accurate electromagnetic behavior of the material. The situation described emulates the water film that forms over the outer surface of radomes in real scenarios. Results computed by the analytical case are overlapped with the HFSS simulations in Fig. 6 for a slab of water without the radome. Results show good agreement between the two methods. In Fig. 6a, an increase of the reflectance with the frequency, and with the thickness of the slab, is noticeable. In contrast, in Fig. 6b the transmittance is higher at lower frequencies and for thinner water films. The absorption in Fig. 6c was computed using Eq. (20) as a function of the known quantities R and T, because they are directly computed or simulated. The absorption is lower at S-band frequencies and increases approaching X band. The highest absorption occurs for the thinnest slab (0.2 mm) of water. Figure 6a shows that by increasing the thickness of the slab, the reflectance rises while the transmittance decreases, because the second term of the denominator of Eq. (15) becomes dominant. The opposite case occurs when the thickness of the layer is reduced.

Correction algorithm

This paragraph describes the procedure to estimate the transmittance that occurs through a wet radome based on the fact that the reflectance is directly measured (reflectometer) and that the absorptance can be calculated. Such an algorithm will be applied in Part II to estimate the attenuation through an operative radome. By this assumption it follows that Eq. (20) can be rewritten as

$$T_{r+w}^{\text{true}} = 1 - R_{r+w} - A_{r+w}, \tag{21}$$

where the subscript means radome + water, to indicate a wet radome. Equation (21) represents the exact (true) solution to evaluate the transmittance, if reflectance and absorptance are known. The proposed technique employs a reflectometer, which means that the reflection coefficient is always known. This is not true for the absorption in cases when it occurs. To overcome this drawback, an approximation that requires the absorptance to be evaluated separately is necessary. Since the absorption is mostly due to the presence of water over the radome, as droplets/rivulets or water film formation, Eq. (21) is rewritten in its approximate form as

$$T_{r+w}^{\text{est}} \approx 1 - R_{r+w} - A_w. \tag{22}$$

In Eq. (22) the superscript "est" stands for estimated, while the term A_w is the computed absorptance as a result of water without radome only. Equation (22) can be employed instead of Eq. (21) when the radome absorption is small, or because the radome stackup is, in general, unknown. If the radome stackup is not known, then the related absorption cannot be computed. It is important to note that the attenuation is different from the absorption. Attenuation is quantified by the transmission loss (TL $= 1/T$), which represents what is not transmitted, because both the signal is absorbed and part of it is also reflected. If a sample of a flat radome is available, then the absorption can be measured by using the technique shown in Fig. 1a. However, it is rare that a separate sample of the same radome material actually employed in the radar is available; thus, in this paper the radome stackup will be assumed to be unknown. The following algorithm allows for the estimation of the transmittance through a wet radome by ignoring the

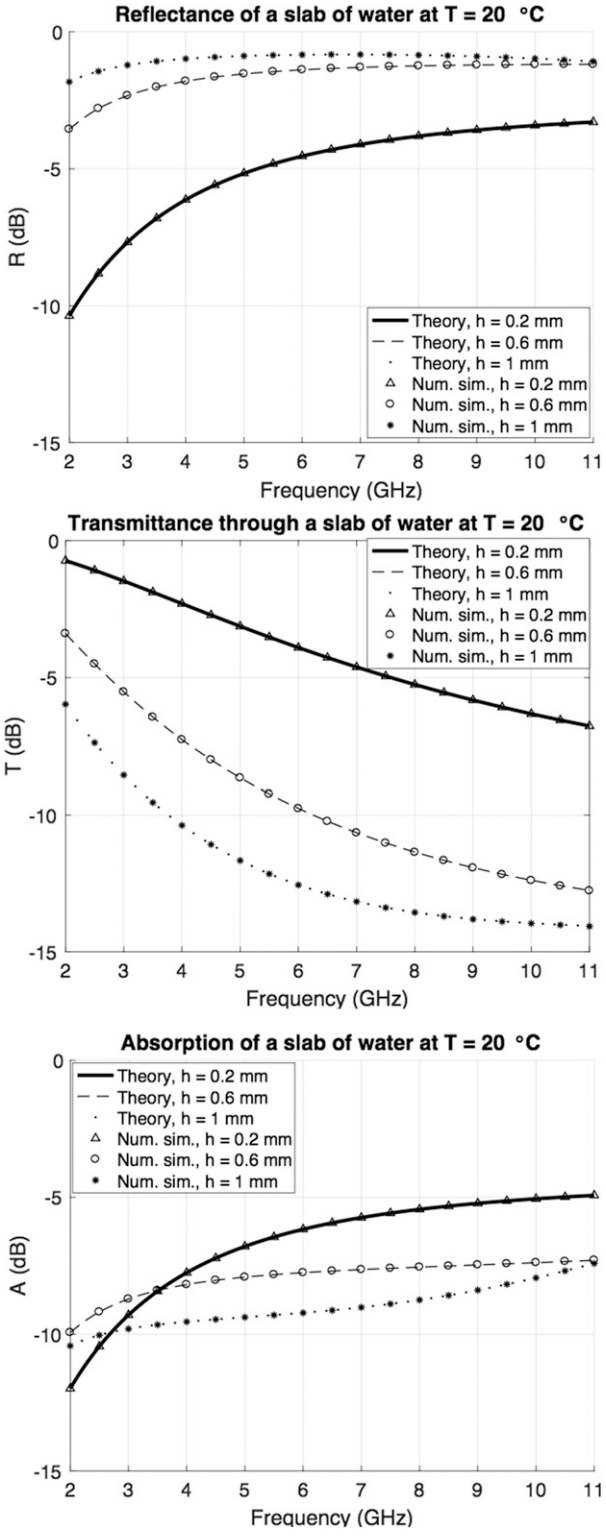

FIG. 6. A comparison between the analytical model and HFSS simulations for different thicknesses of a slab of water (no radome included) at 20°C: (a) the reflectance, (b) the transmittance, and (c) the absorptance.

absorption occurring inside the radome itself. It will be shown that the only quantity necessary is the term A_w, which depends on the water distribution over the radome. This procedure is described below for cases when water distributes as a film or as droplets.

1) WATER FILM

When water distributes as a film, the thickness of the slab depends on the rain rate R. For a spherical radome, the thickness is given by Gibble (1964)

$$t = \sqrt[3]{\frac{3\mu R a}{2\rho g}} \tag{23}$$

where μ is the dynamic viscosity of the water (kg m^{-1} s^{-1}), R is the rain rate (m s^{-1}), a is the radius of the spherical radome (m), ρ is the density of water (kg m^{-3}), and g is the gravitational acceleration (m s^{-2}).

Once the thickness is calculated, the reflectance and transmittance through a slab of water can be computed by using Eqs. (14) and (15). Then by reordering Eq. (20) for A, the absorptance can be found. The absorption derived is the term A_w to employ in Eq. (22). Since the reflectance for the radome + water film stackup (or wet radome) is directly measured by the reflectometer, and the absorption of the water film (no radome) is known for a specific rain rate, then the transmittance through the wet radome can be estimated by using Eq. (22).

To validate this algorithm, simulations in HFSS were performed. The PX-1000 radome, with a radius of 1.1 m, was used for the simulation. The water thickness was computed for such a radius by using Eq. (23). In Table 4 the thicknesses calculated at different rain rates are shown. The radome stackup is listed in Table 3, and the performance in dry conditions is shown in Figs. 1c and 1d. First, a simulation of this radome was performed by adding a layer of water at 20°C. In this way the true value of transmittance T_{r+w}^{true} was identified for the purpose of comparison. Second, using Eqs. (14) and (15), the reflectance R_w and transmittance T_w through a slab of water without the radome were computed analytically. Then, the absorption A_w is calculated by reordering Eq. (20). Finally, the transmittance of the wet radome T_{r+w}^{est} is estimated by Eq. (22). In Fig. 7, the comparison between T_{r+w}^{true} and T_{r+w}^{est} is shown for different water layer thicknesses. In the third column of Table 4, the maximum relative error of the transmittance is presented. The relative error is computed as the absolute value of the difference between T_{r+w}^{true} and T_{r+w}^{est}, normalized with respect to T_{r+w}^{true}. The maximum relative error occurs at different frequency points for the various thicknesses in the band 8.5–11 GHz. For all the cases, the error is below

TABLE 4. The water film thicknesses calculated for different rain rates. The third column shows the maximum relative error between the true value of transmittance, directly measured by simulation in HFSS, and the approximated value computed by Eq. (22) in the frequency band considered. In the fourth column, the relative error (previously described) occurring at 9.55 GHz is shown. In the last two columns, a comparison of the attenuation found in the current study with Frasier et al. (2013) is presented.

Rain rate (mm h^{-1})	Thickness (μm)	Max error (%)	Error at 9.55 GHz (%)	Mancini (dB)	Frasier et al. (dB)
5.3	63	4.4	0.72	2.15	1.7
20	98.06	3.59	0.03	3.3	2.5
40	123.5	3.78	0.51	4.1	3.1
60	141.4	4.07	0.83	4.6	3.5
120	178.2	4.56	1.32	5.6	4.4
200	211.3	4.81	1.62	6.5	5.2

5%, demonstrating that the approximation does not introduce a large bias in the computation of the transmittance. This is because the absorption of the dry radome is low. In the fourth column of the table, the relative error at the frequency at which the radome was designed, 9.55 GHz, is presented. In the last two columns, a comparison of the true value of the attenuation ($1/T_{r+w}^{\text{true}}$) found in this study and the one computed by Frasier et al. (2013) is shown. Two observations can be made. First, the attenuation found in this paper overestimates the one computed using Frasier et al. (2013). Second, the difference between the attenuation level increases as the rain rate rises. The discrepancy between the two studies depends on the radome stackup employed, the radome conditions (not mentioned in Frasier et al. 2013), and considerations about the water temperature can be also fundamental (Fig. 5). In addition, in Fig. 6 of Frasier et al. (2013), it is shown that the attenuation computed by Frasier et al. underestimates the other studies used for the purpose of comparison. Regarding the second observation, Frasier's formula was found to fit Marshall–Palmer and WSR-88D up to a rain rate of 20 mm h^{-1} (Frasier et al. 2013). At higher rain rates, the equation employed by Frasier might need adjustment of the parameters.

2) DROPLETS

When water distributes as droplets rather than as a continuous film—for instance, in cases when the radome

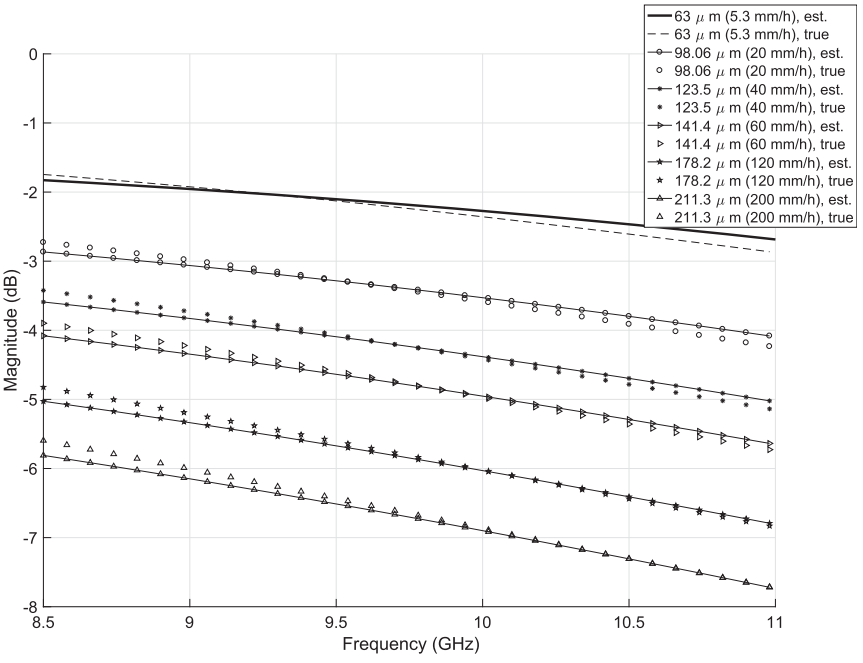

FIG. 7. A comparison between the true and estimated transmittances for different water film thicknesses. In the legend the equivalent rain rates for each thickness are shown in parentheses.

is made with a superhydrophobic coat—the drop size distribution (DSD) must be computed. The gamma distribution, also used in Salazar-Cerreno et al. (2014), was chosen to calculate the DSD:

$$n(D) = N_0 D^u e^{-\Lambda D},$$
$$\Lambda = 4.2R^{-0.21},$$
$$N_0 = 8 \times 10^3, \text{ and}$$
$$u = -0.016\Lambda^2 + 1.213\Lambda - 1.957, \quad (24)$$

where D is the droplet diameter and R is the rain rate. The number of droplets derived from Eq. (24) is listed in Table 5 for 4, 5, and 6.3 mm h^{-1} rain rates. A similar algorithm to the one used in the water film scenario is employed to compute the transmittance through a radome wetted with droplets. A simulation in HFSS was performed to evaluate the absorption (A_w) through a population of raindrops obtained by Eq. (24), and scaled by a factor of 20. In such a simulation, the droplets were designed to be semispherical, in order to reproduce the formation occurring over a hydrophobic surface. These droplets were randomly placed on a surface of dimension $\lambda \times \lambda$ (at 9.55 GHz). Rivulets were not considered for this study. However, because of the casual placement, it was possible that some droplets coincidentally represented an approximation of a rivulet. Three rounds of simulations were performed for each rain rate listed in Table 5. The first scenario for each rain rate considers the droplets without the radome in order to compute A_w. The term A_w, so obtained, is the average of the three rounds executed at the same rain rate, in which each round considered a different random placement of the droplets. In the second simulated scenario, the same random placement of droplets corresponding to each of the previous rounds was used to repeat the test adding the radome stackup (Table 3), in order to evaluate T^{true}_{r+w} and R_{r+w} for the purpose of comparison. In this way it is possible to derive T^{est}_{r+w} from A_w as a result of the first scenario and from R_{r+w} from the second scenario. In real applications R_{r+w} is directly measured by the reflectometer. In this way all the quantities necessary to find T^{est}_{r+w} are identified [Eq. (22)]. In Fig. 8a the results are shown by comparing the true and the estimated transmittances, averaged over the three rounds for each of the rain rates. The results show greater discrepancy between the true and the estimated values than occurred in the water film scenario. This is probably due to the scattering generated by the droplets. The presence of scattering is noticeable in the peaks in Fig. 8a. The resulting peaks change when the transmittance is estimated by using A_w, which does not consider the radome, from when it is directly computed (T^{true}_{r+w}) with the radome included. Since the scattering

TABLE 5. The DSD calculated at different rain rates, scaled by a factor of 20. Also shown is the relative error, averaged in the 8.5–11-GHz frequency band, and the relative error (before average) at 9.55 GHz, between the true and the approximated values of the transmittance.

Rain rate (mm h^{-1})	1 mm	1.5 mm	2 mm	2.5 mm	Avg error (%)	Error at 9.55 GHz (%)
4	19	8	3	1	7.97	6.94
5	20	9	3	1	9.05	6.35
6.3	25	20	4	1	9.03	6.1

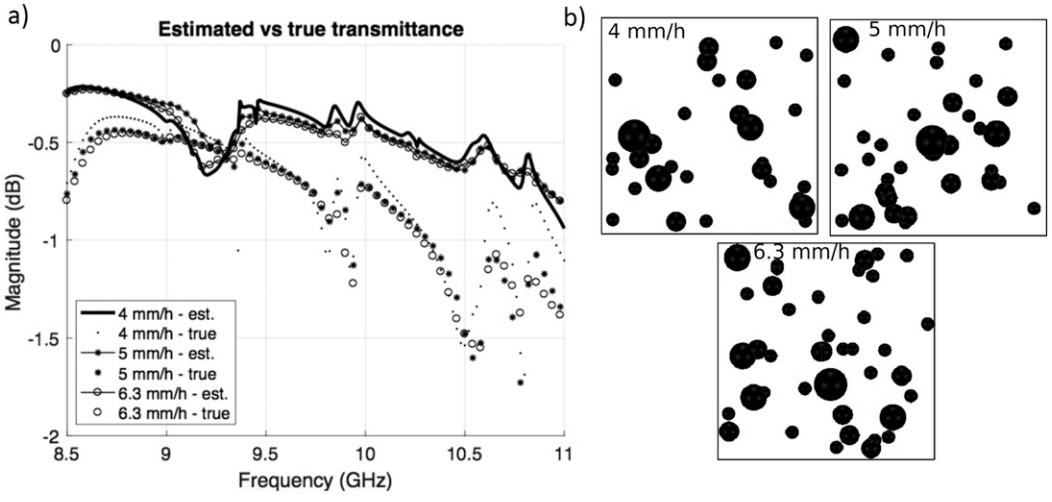

FIG. 8. (a) The comparison between the true and the estimated transmittance through a radome wetted with droplets. (b) The random droplet distribution corresponding to round 1 of the simulation for 4, 5, and 6.3 mm h^{-1} rain rates.

TABLE 6. Comparison between the one-way attenuation (dB) simulated at 9.55 GHz and the one computed by using Trabal's method.

Rain rate (mm h^{-1})	Mancini	Trabal
4	0.6	0.67
5	0.63	0.76
6.3	0.64	0.86

as a result of the droplets is weak, the presence of the radome alters the field distribution in the two scenarios. Because of the presence of such peaks, it is more meaningful to show the relative error of the estimated transmittance as the average over the 8.5–11-GHz frequency range than presenting the maximum value. In Table 5 the mean of the relative error and the relative error of the transmittance occurring at 9.55 GHz are shown. In Fig. 8b the disposition of the raindrops across the surface is shown for each rain rate corresponding to the first simulated round.

To conclude the study of water formation as droplets, a comparison was made between the one-way attenuation obtained by the true value of the transmittance (T_{r+w}^{true}) and the one computed as in Trabal et al. (2008). This is shown in Table 6. The one-way attenuation for the rain rates considered are in the same range as the ones found in Trabal et al. (2008). The difference between the results of the two studies is a consequence of the DSD chosen and the scaling factor of the DSD. Furthermore, no information about the radome condition used in Trabal et al. (2008) was provided.

4. Experimental setup

This section presents the setup and key components of the proposed instrument. Details about the antenna used as a probe and reflectometer operating in time domain are also discussed.

a. Probe: Dielectric rod antenna

To fully characterize the radome surface using the proposed technique, the antenna employed as a probe requires a low size and a narrow beamwidth. An antenna beamwidth is measured at the half-power (−3 dB) point of the main beam. A narrow beamwidth enables high spatial resolution of the radome measurements and makes it suitable for the investigations proposed in this paper. However, if a narrow-beam probe is used, then the area of the radome sampled by the probe is much smaller than the one sampled by the radar antenna, which operates in the near field at the distance of the radome. For the case proposed, the sampling area of the probe is only 9% of the area sampled by the parabolic

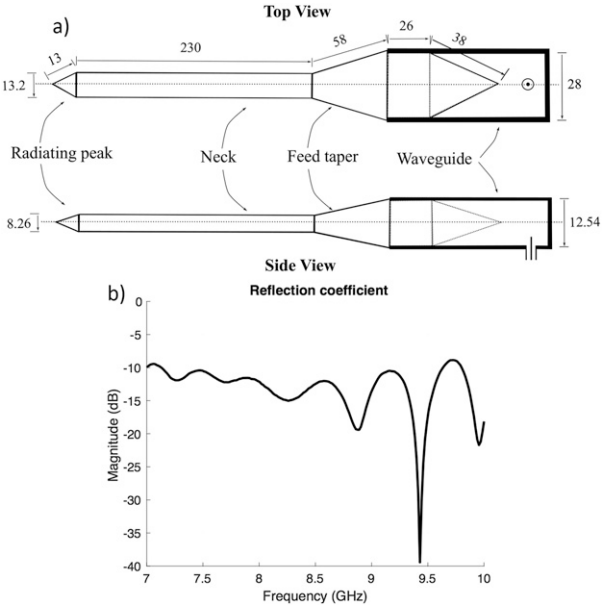

FIG. 9. (a) Two illustrations showing the dielectric rod dimensions (mm), at top and side views. The part of the rod that is located inside the waveguide is indicated (dashes). (b) The reflection coefficient of the rectangular waveguide with the dielectric assembled.

reflector. A wider area can be sampled if a probe with a larger beamwidth is designed, but it comes at the expense of the spatial resolution. It is left to the user, based on the primary purpose of the application to define this trade-off. Low weight and small transversal area are key features for easy implementation in operational radars. A small size probe is necessary in order to minimize the signal blockage. The type of antenna selected by the user for conducting this research is the dielectric rod antenna. In the past dielectric rod antennas were used for diverse applications by Mueller and Tyrrell (1947), Watson and Horton (1948), Kobayashi et al. (1982), Studd (1991), Zucker and Croswell (2007), and Stroobandt (1997).

The dielectric rod antenna belongs to the family of surface-wave antennas and is obtained by placing a dielectric rod in the waveguide aperture. The portion of the dielectric located inside the waveguide is called the feed taper. The feed taper has the function of providing impedance matching at the waveguide–dielectric transition, increasing the efficiency of excitation. The body taper, another part of the dielectric, mainly reduces the level of sidelobes and also increases the bandwidth. The terminal taper, located at the tip of the dielectric, improves the impedance matching between the dielectric and the air, decreasing the reflected surface-wave level (Zucker and Croswell 2007). The length of the neck of the dielectric (Fig. 9a) determines the gain and beamwidth. However, if there is not sufficient headroom

between the radar feed and the radome, or if a smaller impact of the probe on the radar antenna is desired, then it is possible to decrease the size of the probe by employing miniaturizations techniques (Volakis et al. 2010, 160–180). In general, a smaller version of the dielectric rod can be obtained by choosing a material with higher dielectric constant. If the beam of the probe is narrow, it is possible to use this antenna as an RF probe for characterization of a smaller radome panel. A narrow beam is more easily confined in the radome sample and no fringing effects from the borders occur (Díaz et al. 2015). The far-field distance of this kind of antenna is 2–3λ (λ = 3.2 cm at 9.4 GHz). Considerations about the far-field distance of the probe are important, because the analytical models presented in this paper are based on the assumption of a plane wave propagating, which is valid only in the far-field region of the probe. Thus, all the devices under test must be located in the far field of the probe.

The dielectric rod antenna employed as a probe needs to be customized in order to operate at the same frequency band as the radar. In the present research, the probe employed for radome characterization was composed of a rectangular waveguide (commercially available) and a dielectric rod optimized to operate at X band (designed in HFSS and in-house 3D printed). The acrylonitrile butadiene styrene (ABS), which is a common thermoplastic polymer, is the material the authors had available for 3D printing the dielectric rod. The probe was then constructed by wedging the dielectric rod inside the waveguide. In Fig. 9a illustrations of the top and side views of the dielectric rod employed in this study are shown. In this paper an H-band rectangular waveguide was employed to operate in the portion of the frequency spectrum that overlaps with X band (8.2–10 GHz). The reason for this was because an X-band waveguide was not available at the time of the experiments. In Fig. 9b the reflection coefficient is plotted. A summary of the electric performance of the antenna is listed in Table 7 and is based on a plot presented in Mancini et al. (2017). The gain of the probe, measured in the far-field chamber, is 17.5 and 19 dB at 8.8 and 9.8 GHz, respectively.

TABLE 7. The performance of the RF probe at 9 and 10 GHz, for the H and E planes.

Parameter	H plane, 9 GHz	E plane, 9 GHz	H plane, 10 GHz	E plane, 10 GHz
Beamwidth (°)	20	20	15	15
Sidelobe level (dB)	−12.9	−12	−9.9	−9.3
Cross polarization (dB) at $\theta = 0°$	−33	−37	−33.2	−40

b. *Reflectometer*

The novelty of this study is that the radome characterization is performed by measuring the reflection coefficient. To accomplish this goal, a vector network analyzer (VNA) reflectometer R140 by Copper Mountain was employed. This device has several applications, including adjustment and testing of antenna–feeder devices, and is used in automated measurement systems. The operative frequency range of the reflectometer is 85 MHz–14 GHz. It operates with the assistance of an external computer that also powers the device. The block diagram of the reflectometer (VNA R140) is shown in Fig. 10. The main components of the VNA are a source oscillator, a local oscillator, a directional coupler, and a digital signal processor (DSP). The output of the reflectometer (test port) is the incident signal. The two-channel receiver filters and digitally encodes the signals. Additional processing of the signals is performed in the DSP. The reflection measurement is performed by comparing the received (reflected) signal with the source signal. An important aspect of the reflectometer is the ability to operate in the time domain using the time domain gating analysis, which will be discussed next. The pulse repetition frequency of the VNA R140 is 30 KHz. The peak power was set to −10 dB*m* for the measurements subsequently described. The frequency accuracy of the VNA is ±25 PPM. Other information about the measurement accuracy is summarized in Table 8.

c. *TDG*

The concept of time gating is to apply a filter in the time domain. Time gating is distance or spatial filtering, which means that only data from a certain range gate are processed. TDG was employed in the past by various researchers for disparate applications. For example, Archambeault et al. (2006) used it to remove discontinuities or reflections in a free-space context and for tuning purposes. Burrell and Jamieson (1973), Wayapattanakorn and Parini (1993), and Fordham (2010) employed the TDG to measure radiation patterns, while Ghodgaonkar et al. (1989) and Zhao et al. (2006) used this filter for calibration in free-space measurements.

1) TIME DOMAIN TRANSFORMATION

The Fourier transform is the operation necessary to switch from frequency to time domain representation, and it applies to continuous signals. The VNA, or reflectometer, performs a digital Fourier transform, since it works with discrete data, and the measured signal is a sampled representation of the continuous signal. Consequently, a problem of this operation is

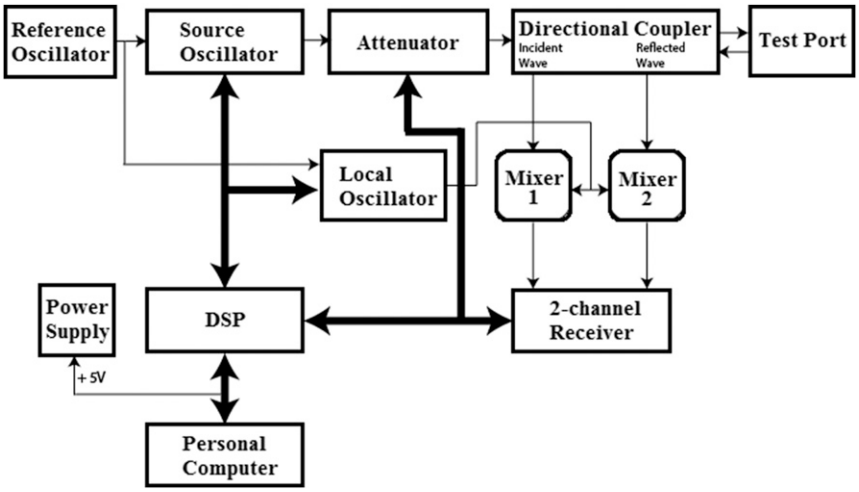

FIG. 10. The block diagram of the reflectometer (R140).

the presence of aliasing. Aliases are undesired replicas of the same signal distributed periodically in the time axis. It is fundamental to operate in an environment free of aliases in order to make a correct interpretation of the measurements. The R140 is implemented in order to always represent data free from aliases. Another unwanted effect is produced by the truncation generated by the frequency-finite representation of a signal, which in the real world is not limited in frequency, and thus sidelobes are introduced in the time domain. These ringing effects are described by a Sinc(t) function and they cannot be totally eliminated (Agilent 2012). To enhance the time domain response, a window can be applied in the frequency domain to control the sidelobes in the time representation resulting from the truncation process. In the present study, a normal type of Kaiser window with −44 dB of sidelobe level was used.

The gate can be thought of as a filter in the time domain. However, the operation of ''gating'' is actually applied in the frequency domain by defining the start and stop gate times that determine the dual-frequency gating function. Dunsmore (2008) conducted a study to evaluate errors in the time domain response caused by inaccurate positioning of the gate around the desired region. Other limitations of the gating function are described in Agilent (2012).

2) RANGE AND RESOLUTION

The process of representing a continuous signal by a sampled (discrete) version of itself produces periodic repetitions. These unwanted replicas are called aliases and they are located at multiples of $1/B$ s. In this specific context, the band B is the frequency range selected to represent the signal in the frequency domain. The alias-free range is also called the unambiguous range. It is the maximum (time or distance) range in which replicas of the signal are not visualized. Defining $B = f_{\max} - f_{\min}$, with $f_{\min}$ and $f_{\max}$ being the start and stop frequency, respectively, the time range can be computed as

$$T = \frac{N-1}{B}, \tag{25}$$

where N is the number of measurement points. For example, by choosing $N = 61$ and $B = 3$ GHz, a time range of 20 ns is achieved. The ambiguity range is given by

$$R_{\max} = \frac{cV_f T}{2}, \tag{26}$$

where c is the speed of light and V_f is the cable velocity factor. The ambiguity range is 3 m if $V_f = 1$ and $T = 20$ ns. The factor 2 in the denominator is necessary to take into account the round trip of the signal.

TABLE 8. Measurement accuracy of the VNA R140 reflectometer.

Measurement	85 MHz–4.8 GHz	4.8–14 GHz
−15 to 0 dB	±0.4 dB/±4°	±0.5 dB/±5°
−25 to −15 dB	±1.2 dB/±8°	±1.5 dB/±10°
−35 to −25 dB	±4.0 dB/±22°	±5.0 dB/±29°

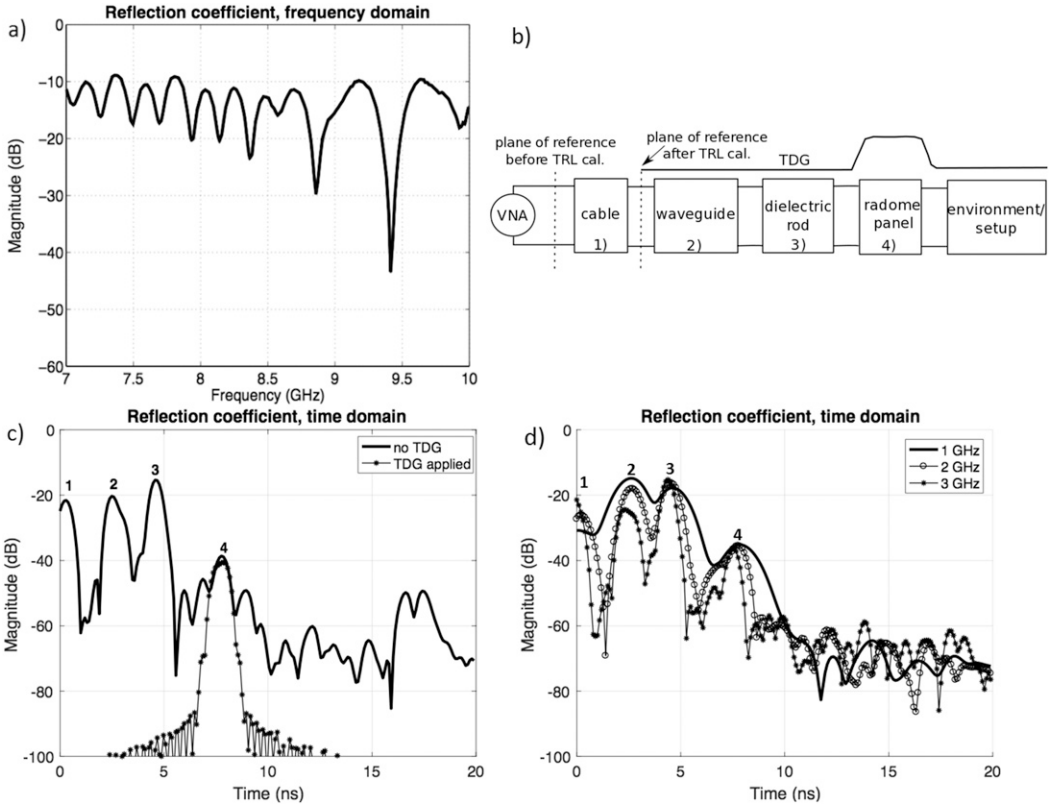

FIG. 11. An example of reflection responses generated by the laboratory setup in the (a) frequency and (c) time domains, obtained with the antenna pointing at $\theta = 0°$. (b) A block diagram of the elements causing the reflections (peaks 1–4). (d) The resolution comparison in the time domain for different frequency bands. In the time domain plots, peaks 1, 2, and 3 are noticeable because of the cable, waveguide, and dielectric rod impedance mismatches, respectively.

The range resolution is the capability of the reflectometer to resolve two responses close (in space or time) to each other. It is calculated as (Agilent 2012)

$$\Delta R = \frac{\Delta t c V_f}{2}, \tag{27}$$

where Δt is 50% points of the impulse width (time). It is defined as

$$\Delta t = \frac{1.95}{B}. \tag{28}$$

The constant 1.95 is related to the choice of a normal Kaiser window (Table 1-3 of Agilent 2012). There is no specific reason for the choice of the Kaiser window of type normal for the experiments performed in this paper. For a 3-GHz bandwidth, the Δt is equal to 0.65 ns, and the range resolution is 9.75 cm. From Eqs. (27) and (28), it is clear that increasing the frequency range decreases the minimum distance at which two targets must be located in order to be resolved.

In the proposed study, TDG was necessary to more accurately measure the reflections produced from the radome without contamination from the reflections generated by the surrounding environment. The implementation of the TDG to the laboratory setup (Fig. 13a) used to validate the proposed concept is discussed. With the dielectric antenna placed at $\theta = 0°$, the measured reflection coefficient is plotted in Fig. 11 in the frequency (Fig. 11a) and time (Fig. 11c) domains. The frequency plot shows the antenna bandwidth affected by the reflections coming from the radome panel immediately above it, parts of the setup, and the surrounding external environment. Clearly, it is not possible to separate and establish which reflections are due to the radome panel (useful part) and which ones are due to the rest of the environment (undesired reflections). The time domain plot shows the reflections (peaks) versus the ''distance'' between the VNA and the target in time. The electromagnetic distance, expressed in time, takes into account the guided propagation of the signal inside the RF cable, the waveguide and dielectric rod of the antenna, and the

free-space propagation. A block diagram of the elements causing the reflections is shown in Fig. 11b.

Analyzing the time domain response without applying the TDG, represented by the thick solid curve in Fig. 11c, it is possible to distinguish the reflections and their related sources, since they are expressed versus the distance in time. The three dominant peaks (1, 2, and 3), located approximately at 0.3, 2.5, and 4.6 ns, respectively, are generated by impedance mismatches. The reference plane, which corresponds to 0 ns, is located at the port of the reflectometer, as shown in Fig. 11b. An open, short, and load calibration is necessary to remove the reflection (peak) resulting from the cable. Peak 1 is created by the cable impedance mismatch (no calibration applied). Peak 2 is due to the impedance mismatch introduced by the waveguide. Peak 3 is produced by the waveguide–dielectric rod junction. Peak 4, located at circa 7.8 ns, represents the reflections generated from the radome placed at 12.5 cm above the antenna. Other minor peaks are visible at time >7.8 ns and are the result of multiple contributions from the environment that are received together. The plot in the time domain was obtained using a frequency span of 3 GHz, since in the frequency plot (Fig. 11a) a 3-GHz range (7–10 GHz) was used to display the curve. Defining the start and final cutoff times of the filter, equal to 7.5 and 8 ns, respectively (t_{d1} and t_{d2}, respectively, in Fig. 1b), the result is the thin solid curve with asterisks in Fig. 11c. By eliminating all the undesired peaks, a purer reflection coefficient in the frequency domain (no fluctuations) is obtained. Figure 11d presents a comparison of resolutions in the time domain for different frequency spans in the laboratory setup scenario.

The TDG is an important technique for removing undesired reflections. Such reflections are generated by impedance mismatches, and it is fundamental to understand what causes them. Impedance mismatches create loss of energy of the incident signal because part of it is reflected. Furthermore, impedance discontinuities can obscure the response of the subsequent mismatches, because the energy reflected from the first impedance mismatch never reaches the following ones. Such an effect is called masking (Agilent 2012). The factors that contribute to generating discontinuities in the proposed research are the presence of cable, waveguide, and dielectric rod (previously described). Their effects are presented in Fig. 12. In the figure, three cases are considered: the first using an ordinary RF cable for the antenna–reflectometer connection with the open, short, and load calibration applied (dotted curve in top panel; thick solid curve in bottom panel); the second using the cable but without applying the open, short, and load calibration (thick solid curve in top panel; thin curve with open circles in bottom panel); and the last case without using the cable but connecting the VNA directly to the antenna and applying the open, short, and load calibration (thin curve with asterisks). These three cases are presented in both frequency and time domain. In the frequency plot, the cases were compared with the reflection coefficient of the antenna measured with a Keysight performance network analyzer (PNA; N5225A) for the purpose of reference. A PNA is a very accurate device for performing measurements of linear characteristics of RF components and devices. The oscillations produced by the RF cable (thick solid curve in top panel; thin curve with open circles in

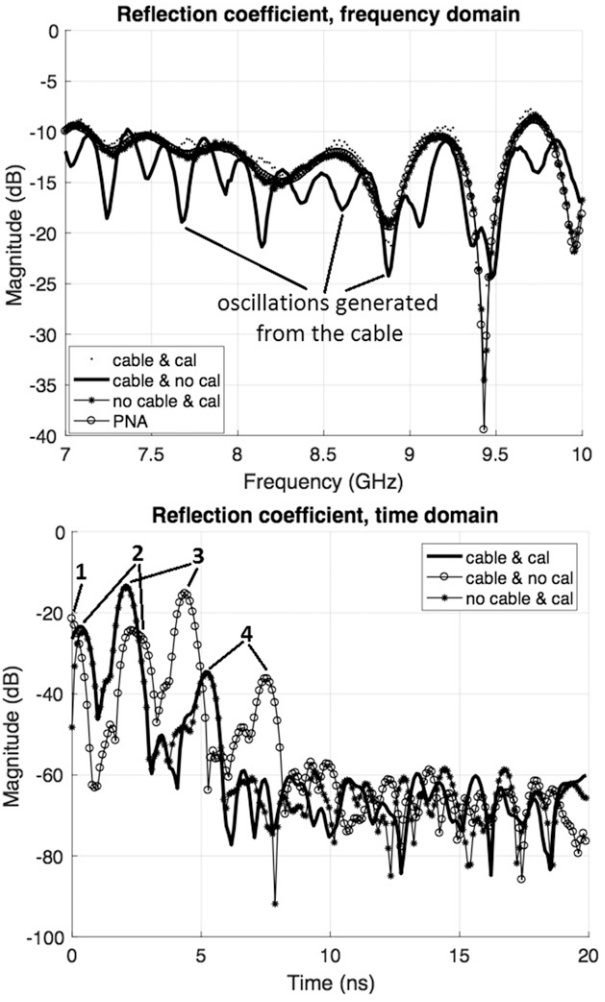

FIG. 12. The open, short, and load calibration effects using a 3-GHz bandwidth in the (top) frequency and (bottom) time domains. Peak 1 corresponds to the cable mismatch, which is present only in the thick solid curve in the top panel and the thin line with open circles in the bottom panel. Once the calibration is applied, peak 1 moves to the negative axis of the time. As consequence of the calibration, peaks 2–4 in the thin curve with open circles (bottom panel) are shifted to the left on the plot (thick curve and thin curve with asterisks).

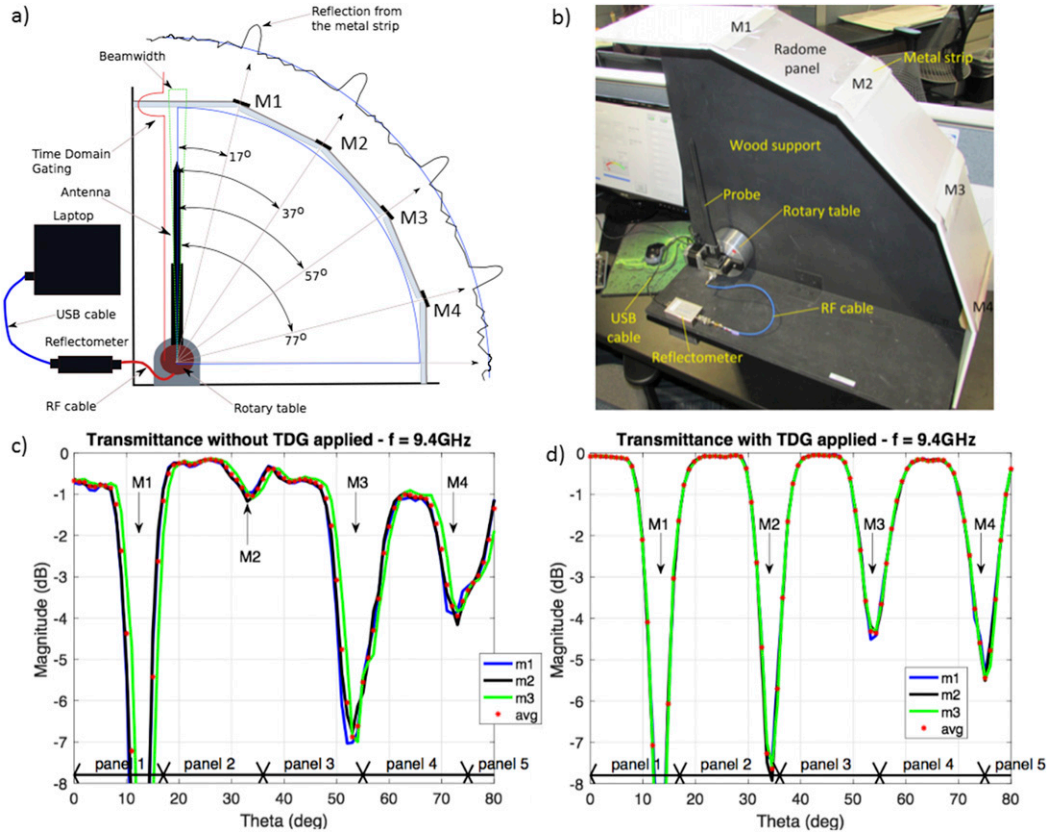

FIG. 13. The setup for the laboratory experiment employing the proposed technique using four metal strips as reference. (a) A graphic representation of the setup, including the probe and reflectometer. (b) A photograph of the setup, with the probe and reflectometer. (c) The transmittance without TDG applied. (d) The transmittance with TDG applied.

bottom panel) are clearly noticeable. When applying the open, short, and load calibration, the plane of reference is shifted to the output of the cable, and then the cable reflection (peak 1) is moved to the negative axis of the time. By removing peak 1, the curve that was obtained by using the cable with an open, short, and load calibration applied (dotted curve in top panel; thick solid curve in bottom panel) matches with the thin curve with asterisks, where no cable was used, and it also matches with the reflection coefficient, in the frequency domain, of the antenna measured with a Keysight PNA.

The effects caused by the impedance mismatches generated from the cable, waveguide, and dielectric rod have been discussed and shown in the frequency and time domains. Benefits resulting from the open, short, and load calibration have also been mentioned.

5. Laboratory experimental results

To validate the concept discussed in section 3 (Fig. 3), a laboratory setup was built to enable the testing that provided preliminary results. This section is divided into two parts. The first part describes the measurements obtained from a setup composed of flat radome panels (Fig. 13). The second part presents the results obtained from the modified setup (Fig. 14).

In Figs. 13a and 13b, a schematic representation and a photograph of the setup are shown. The laboratory setup is composed of five radome panels arranged to approximate a quarter of the circumference. The rotary motor with the probe mounted on it is located at the origin of the circumference. The panels are placed abutting each other, leaving small air gaps between each other. These air gaps are located at $\theta = 17°, 37°, 57°$, and 77° with respect the initial position of the rotary motor, as shown in Figs. 13a and 13b. To keep the radome panels in a stable position above the antenna and to secure the rotary motor to a fixture a wooden support was used. Because of imperfections in the setup, the distance between the antenna and each panel is not identical.

The radome panel is made of foam as an inner layer (6.62 mm) and teflon as a skin layer (0.53 mm). In

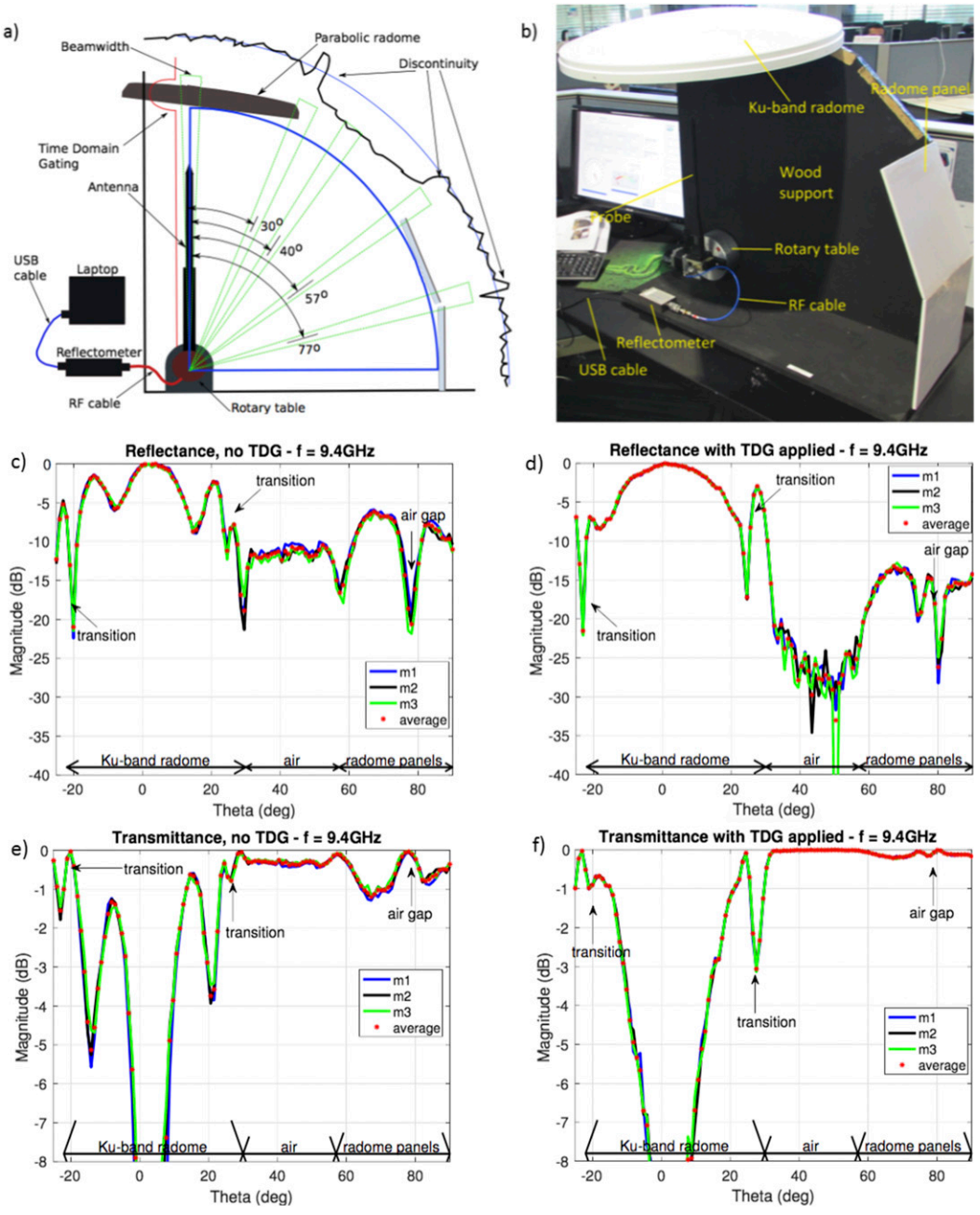

FIG. 14. The modified laboratory setup employing a Ku-band radome: (a) graphical representation, including the probe and reflectometer, and (b) a photograph of the setup, with the probe and reflectometer. (c) The reflectance without applying the TDG. (d) The reflectance with the TDG applied. (e) The transmittance without applying the TDG. (f) The transmittance with the TDG applied.

Fig. 13a the antenna is placed at the start position (broadside; $\theta = 0°$) of the rotary motor, the probe beamwidth is shown in green, the TDG is displayed in red and centered at the radome location, and the predicted results for the reflection measurement are shown. Both a flat response of the reflection coefficient from the radome panel and a strong reflection coefficient peak generated from each metal strip located at the junction between two consecutive panels are expected.

The setup was modified for the second part of this study. The reason for this modification was to characterize an operational radome that is not flat but presents a curvature. Three of the radome panels were removed and a Ku-band radome (also applicable at

X band) replaced them, leaving a large air gap between the radome and the remaining two panels. The Ku-band radome has a circular shape with a 60-cm diameter and presents a small angle curvature from the center to the peripheral area. However, at the borders the termination is cornered, so it can be mechanically fixed to the reflector. In Figs. 14a and 14b, a schematic view and a photograph of the modified setup are presented, respectively, showing the predicted behavior for the reflection coefficient as in the previous setup.

The TDG width is defined by the start and stop times. For the following experiments, they were set to 7.5 and 8 ns, respectively. Considering that the distance between the probe and the panel was slightly different because of fabrication imperfections of the setup, the TDG width was set in order to capture only the reflections from each single panel, making sure that all radome panels fell inside the TDG width. This was done by performing initial tests with larger time spans for the gating. These experiments produced consistent results; they were not reported here for the sake of brevity.

A LabVIEW interface was created to have a fully automated system. The measurement criterion is identical for both of the setups employed. First, the rotary motor rotates the RF probe to an angle with increments (or resolution) dictated by the user (1° for this study). Then a sample is taken. This is repeated until the final designed angle (i.e., 80°) is reached. During the tests the probe did not move while the sample was taken. The measurements were repeated three times for each scenario and compared with the average.

a. Case 1: Five-section uniform radome

This section describes the results obtained from the laboratory setup shown in Fig. 13. Measurements of the reflections are plotted at 9.4 GHz, using a 3-GHz bandwidth (7–10 GHz) in order to have good resolution in the time domain. The experiments were performed three times under the same conditions to assure the reproducibility of the experiment. The measurements were then compared with the average. In Figs. 13c and 13d, m1, m2, m3, and avg represent the three measurements and the related average, respectively. The purpose of these experiments was mainly to validate the dielectric antenna and the reflectometer, with TDG applied, as a system to evaluate the effect introduced by the radome in terms of reflections. In particular, the goal was to prove that the TDG is a fundamental analysis to remove undesired reflections and to improve the measurement quality (Fig. 11c). In addition, while conducting experiments when varying transitions existed between radome panels, the measured results show the effect of the discontinuities, mainly produced by diffracted fields. Diffracted fields are difficult to see with a continuous interface. Metal strips were used to cover the air gaps between the consecutive panels with the purpose of providing reference in the tests, as shown in Fig. 13a. In the first experiment, the TDG was not employed in order to determine whether a reflectance measurement of good quality could be achieved without using the gating in the time domain. Strong reflections (peaks) from the metal strips were expected and therefore could be visualized without TDG. Mancini et al. (2017) showed results of the reflectance normalized with respect to the strongest of the peaks generated from the metal strip. In the current manuscript, the same results are shown in terms of transmittance by applying Eq. (19) and are shown in Fig. 13c. The absorption of the dry radome was neglected. The results presented in Fig. 13c show that the multiple paths generated from other surfaces of the setup affected the measurements considerably by canceling some of the peaks. From Fig. 13c, only the first strip (M1), located at 17°, generates a well-formed peak. The peaks related to M3 (at 57°) and M4 (at 77°) are less pronounced. The peak of M2 (at 37°) is barely visible as a result of a combination of destructive reflections. The peaks M1, M3, and M4 shown in Fig. 13c do not have the same amplitude, partially because the distance from the antenna to each radome panel is not the same. The second experiment was performed in the same condition as the previous one but applying the TDG. In Fig. 13d the computed transmittance is shown. Although the peaks still do not have the same minimum value, they are all well shaped and visible, especially the peak as a result of M2. Diffractions caused by the antenna beam in the transition between the radome panels can still affect the measurement. The diffraction occurs in the junctions between two consecutive panels because the antenna beam is not orthogonal to the radome surface. The results, however, are much improved by applying the TDG, confirming the importance of this filter in this research.

b. Case 2: Ku- and X-band radomes

In this paragraph measurements performed using the setup presented in Fig. 14 are shown at the frequency of 9.4 GHz. To have a complete scan of the Ku-band radome, it was necessary to start the measurements at $\theta = -25°$ (instead of 0° as in the first setup employed). In the tests performed with the modified setup, no metal strip was employed, so the normalization was with respect to the highest level of reflection that occurred at the broadside ($\theta = 0°$). The TDG analysis was not employed for the first experiment. Results are shown in Figs. 14c and 14e for the reflectance and the transmittance. The transmittance was again computed using Eq. (19). As in the case presented in Fig. 13c, this test also required the filter in the time domain in order to improve the quality of

the experiments. In the second test the TDG analysis was applied and a 3-GHz bandwidth (7–10 GHz) was employed to assure good resolution in the time domain. The TDG start and stop times were adjusted to account for the dimensions of the new radome, taking into account its curvature. Results are shown in Figs. 14d and 14f for the reflectance and transmittance. It is valuable to compare the two plots in Figs. 14c and 14d in the range of 30°–60°, where no reflection was supposed to be measured, since it is the air region. In the air region, the value of reflection is higher without applying the filter in the time domain, because reflections from other parts of the setup and the rest of the environment were not filtered out.

6. Conclusions

A novel instrument to characterize the effect of a radome in dry and wet conditions was presented. The proposed instrument enables the RF characterization of a radome surface in any condition, employing a single RF probe, in contrast to conventional methods that require two RF probes. The concept, instrument description, formulation, and initial results were discussed in this manuscript. Additional experiments using the radome of an operational radar at X band, tested under the influence of artificial and natural rain, are described in Part II.

The results discussed in this paper demonstrate the validity of the proposed instrument, highlighting that this technique can provide accurate results when the absorption is negligible (section 3; Fig. 1d). In case of water accumulation on the radome surface, the absorption can be estimated by modeling the water formation as a film or as droplets, as function of the rain rate. To obtain an accurate characterization of the radome, it is necessary to combine the TDG technique with a narrow-beam RF probe. This manuscript provides the most important concepts to better quantify the absorption and transmission loss of a wet radome, and it can be used for real-time measurements of a radar system under the influence of precipitation.

Sufficient headroom between the radar feed and the radome must exist in order to employ this technique in an existing radar. This is one of the main limitations of the proposed method. Such a limitation, however, does not apply to future radar systems, where the radome can be designed to accommodate the probe. Another limitation involves the trade-off between the probe beamwidth to achieve high space resolution and the probe size, which could have an impact on the radiation pattern of the radar, where the narrower the beam is, the higher is the mismatch between the area of the radome sampled by the probe and the radar antenna. These trade-offs need to be taken into account during the probe's design.

Acknowledgments. The authors thank Simon Duthoit, Damon Schmidt, Danny Feland, Valery Melnikov, and the ARRC, NOAA, and SENSR for help and the immediate assistance they provided anytime it was necessary.

REFERENCES

Agilent, 2012: Time domain analysis using a network analyzer. Agilent Technologies Application Note 1287-12, 48 pp., http://literature.cdn.keysight.com/litweb/pdf/5989-5723EN.pdf.

Anderson, I., 1975: Measurements of 20-GHz transmission through a radome in rain. *IEEE Trans. Antennas Propag.*, **23**, 619–622, https://doi.org/10.1109/TAP.1975.1141134.

Antonets, I. V., L. N. Kotov, V. G. Shavrov, and V. I. Shcheglov, 2008: Reflection, transmission, and absorption coefficients calculated for the oblique incidence of an electromagnetic wave on a plate. *J. Commun. Technol. Electron.*, **53**, 363–376, https://doi.org/10.1134/S1064226908040013.

Archambeault, B., S. Connor, and J. C. Diepenbrock, 2006: Time domain gating of frequency domain S-parameter data to remove connector end effects for PCB and cable applications. *2006 IEEE International Symposium on Electromagnetic Compatibility (EMC 2006): Proceedings*, Vol. 3, IEEE, 764–769, https://doi.org/10.1109/ISEMC.2006.1706292.

Balanis, C. A., 2012: *Advanced Engineering Electromagnetics*. 2nd ed. Wiley, 1040 pp.

Bechini, R., V. Chandrasekar, R. Cremonini, and S. Lim, 2010: Radome attenuation at X-band radar operations. *Proc. Sixth European Conf. on Radar in Meteorology and Hydrology (ERAD 2010)*, Sibiu, Romania, National Meteorological Administration, P15.1.

Blevis, B., 1965: Losses due to rain on radomes and antenna reflecting surfaces. *IEEE Trans. Antennas Propag.*, **13**, 175–176, https://doi.org/10.1109/TAP.1965.1138384.

Bohren, C. F., and D. R. Huffman, 1983: *Absorption and Scattering of Light by Small Particles*. 1st ed. John Wiley and Sons, Inc., 530 pp.

Burrell, G. A., and A. R. Jamieson, 1973: Antenna radiation pattern measurement using time-to-frequency transformation (TFT) techniques. *IEEE Trans. Antennas Propag.*, **21**, 702–704, https://doi.org/10.1109/TAP.1973.1140560.

Chang, K.-C., 1985: System performance in rain in a radome-enclosed environment. *Proc. 1985 IEEE Military Communications Conf. (MILCOM '85),* Boston, MA, IEEE, 293–299, https://doi.org/10.1109/MILCOM.1985.4794978.

Cheong, B. L., R. Kelley, R. D. Palmer, Y. Zhang, M. Yeary, and T. Yu, 2013: PX-1000: A solid-state polarimetric X-band weather radar and time–frequency multiplexed waveform for blind range mitigation. *IEEE Trans. Instrum. Meas.*, **62**, 3064–3072, https://doi.org/10.1109/TIM.2013.2270046.

Cole, K. S., and R. H. Cole, 1941: Dispersion and absorption in dielectrics I. Alternating current characteristics. *J. Chem. Phys.*, **9**, 341–351, https://doi.org/10.1063/1.1750906.

Díaz, J., J. L. Salazar-Cerreno, A. Mancini, and J. G. Colom, 2015: Multilayer radome design and experimental characterization of scattering and propagation properties for atmospheric radar applications. *Fifth Conf. on Transition of Research to Operations*, Phoenix, AZ, Amer. Meteor. Soc., 819, https://ams.confex.com/ams/95Annual/webprogram/Paper259871.html.

Dunsmore, J., 2008: Gating effects in time domain transforms. *Proc. 72nd Automatic Radio Frequency Technologies Group*

(ARFTG) Microwave Measurement Symp., Portland, OR, IEEE, 1–8, https://doi.org/10.1109/ARFTG.2008.4804303.

Fenn, A. J., 1997: Measurements of wet radome transmission loss and depolarization effects in simulated rain at 20 GHz. *Tenth International Conference on Antennas and Propagation*, Vol. 1, IEE Conference Publication Series, No. 436, IET, 474–477.

Fordham, J., 2010: Use of time domain gating in spherical near-field measurements. *Proc. 14th Int. Symp. on Antenna Technology and Applied Electromagnetics and the American Electromagnetics Conf. (ANTEM-AMEREM)*, Ottawa, ON, Canada, IEEE, 4 pp., https://doi.org/10.1109/ANTEM.2010.5552375.

Frasier, S. J., F. Kabeche, J. F. I. Ventura, H. Al-Sakka, P. Tabary, J. Beck, and O. Bousquet, 2013: In-place estimation of wet radome attenuation at X band. *J. Atmos. Oceanic Technol.*, **30**, 917–928, https://doi.org/10.1175/JTECH-D-12-00148.1.

Frech, M., 2009: The effect of a wet radome on dualpol data quality. *34th Conf. on Radar Meteorology*, Williamsburg, VA, Amer. Meteor. Soc., P13.15, https://ams.confex.com/ams/34Radar/techprogram/paper_155405.htm.

——, B. Lange, T. Mammen, J. Seltmann, C. Morehead, and J. Rowan, 2013: Influence of a radome on antenna performance. *J. Atmos. Oceanic Technol.*, **30**, 313–324, https://doi.org/10.1175/JTECH-D-12-00033.1.

Ghodgaonkar, D. K., V. V. Varadan, and V. K. Varadan, 1989: A free-space method for measurement of dielectric constants and loss tangents at microwave frequencies. *IEEE Trans. Instrum. Meas.*, **38**, 789–793, https://doi.org/10.1109/19.32194.

Gibble, D., 1964: Effects of rain on transmission performance of a satellite communication system. *IEEE International Convention Record, Part VI*, Seattle, WA, IEEE, 52.

Gorgucci, E., R. Bechini, L. Baldini, R. Cremonini, and V. Chandrasekar, 2013: The influence of antenna radome on weather radar calibration and its real-time assessment. *J. Atmos. Oceanic Technol.*, **30**, 676–689, https://doi.org/10.1175/JTECH-D-12-00071.1.

Hendrix, C. E., J. E. McNally, and R. A. Monzingo, 1989: Depolarization and attenuation effects of radomes at 20 GHz. *IEEE Trans. Antennas Propag.*, **37**, 320–328, https://doi.org/10.1109/8.18728.

Kobayashi, S., R. Mittra, and R. Lampe, 1982: Dielectric tapered rod antennas for millimeter-wave applications. *IEEE Trans. Antennas Propag.*, **30**, 54–58, https://doi.org/10.1109/TAP.1982.1142758.

Kurri, M., and A. Huuskonen, 2008: Measurements of transmission loss of a radome at different rain intensities. *J. Atmos. Oceanic Technol.*, **25**, 1590–1599, https://doi.org/10.1175/2008JTECHA1056.1.

Mancini, A., J. L. Salazar, R. M. Lebrón, and B. L. Cheong, 2017: A novel technique to characterize the effect of rain over a radome for radar applications. *Proc. 2017 IEEE Radar Conf. (RadarConf)*, Seattle, WA, IEEE, 470–475, https://doi.org/10.1109/RADAR.2017.7944249.

——, ——, ——, and ——, 2018: A novel instrument for real-time measurement of attenuation of weather radar radome including its outer surface. Part II: Applications. *J. Atmos. Oceanic Technol.*, **35**, 975–991, https://doi.org/10.1175/JTECH-D-17-0084.1.

Manz, A., L. Handwerker, M. Löffler-Mang, R. Hannesen, and H. Gysi, 1999: Radome influence on weather radar systems principles and calibration issues. Preprints, *29th Int. Conf. on Radar Meteorology*, Montreal, QC, Canada, Amer. Meteor. Soc., 918–921.

Mueller, G. E., and W. A. Tyrrell, 1947: Polyrod antennas. *Alcatel-Lucent J.*, **26**, 837–851.

Pozar, D. M., 2012: *Microwave Engineering*. 4th ed. J. Wiley and Sons, Inc., 732 pp.

Ruze, J., 1965: More on wet radomes. *IEEE Trans. Antennas Propag.*, **13**, 823–824, https://doi.org/10.1109/TAP.1965.1138492.

Salazar-Cerreno, J. L., V. Chandrasekar, J. M. Trabal, P. Siquera, R. Medina, E. Knapp, and D. J. McLaughlin, 2014: A drop size distribution (DSD)-based model for evaluating the performance of wet radome for dual-polarized radars. *J. Atmos. Oceanic Technol.*, **31**, 2409–2430, https://doi.org/10.1175/JTECH-D-13-00208.1.

Schneebeli, M., J. Sakuragi, T. Biscaro, C. F. Angelis, I. C. da Costa, C. Morales, L. Baldini, and L. A. T. Machado, 2012: Polarimetric X-band weather radar measurements in the tropics: Radome and rain attenuation correction. *Atmos. Meas. Tech.*, **5**, 2183–2199, https://doi.org/10.5194/amt-5-2183-2012.

Stroobandt, S. Y., 1997: An X-band high-gain dielectric rod antenna. Katholieke Universiteit Leuven Rep., 37 pp.

Studd, A. C., 1991: Towards a better dielectric rod antenna. *Seventh International Conference on Antennas and Propagation (ICAP 91)*, Vol. 1, IEE Conference Publication Series, No. 333, IET, 117–120.

Thompson, R., and A. Illingworth, 2012: Correcting attenuation in operational radars from both heavy rain and the radome using the observed microwave emission. *Proc. Seventh European Conf. on Radar in Meteorology and Hydrology (ERAD 2012)*, Toulouse, France, Météo-France, 8A.5, http://www.meteo.fr/cic/meetings/2012/ERAD/short_abs/DQ_381_sh_abs.pdf.

Trabal, J. M., I. Zawadski, and D. J. McLaughling, 2008: A method to correct for wet radome attenuation in CASA radars by the use of a contiguous WSR-88D radar. *Proc. Fifth European Conf. on Radar in Meteorology and Hydrology*, Helsinki, Finland, Vaisala, 0287.

Volakis, J. L., C.-C. Chen, and K. Fujimoto, 2010: *Small Antennas: Miniaturization Techniques and Applications*. 1st ed. McGraw-Hill, 448 pp.

Wallace, J. M., and P. V. Hobbs, 1977: *Atmospheric Science: An Introductory Survey*. R. Dmowska, D. Hartmann, and H. T. Rossby, Eds., International Geophysics Series, Vol. 92, Academic Press, 504 pp.

Wang, Y., and V. Chandrasekar, 2006: Polarization isolation requirements for linear dual-polarization weather radar in simultaneous transmission mode of operation. *IEEE Trans. Geosci. Remote Sens.*, **44**, 2019–2028, https://doi.org/10.1109/TGRS.2006.872138.

Watson, R. B., and C. W. Horton, 1948: The radiation pattern of dielectric rods—Experiment and theory. *J. Appl. Phys.*, **19**, 661–670, https://doi.org/10.1063/1.1698188.

Wayapattanakorn, C., and C. G. Parini, 1993: Theoretical and experimental investigations of using time domain gating in antenna pattern measurements. *Eighth International Conference on Antennas and Propagation*, Vol. 1, IEE Conference Publication Series, No. 370, IEE, 327–330.

Zhao, M., J. D. Shea, S. C. Hagness, and D. W. van der Weide, 2006: Calibrated free-space microwave measurements with an ultrawideband reflectometer-antenna system. *IEEE Microwave Wireless Compon. Lett.*, **16**, 675–677, https://doi.org/10.1109/LMWC.2006.885625.

Zhang, G., 2016: *Weather Radar Polarimetry*. 1st ed. CRC Press, 322 pp.

Zrnić, D. S., and R. J. Doviak, 2005: System requirements for phased array weather radar. NOAA/NSSL Rep., 24 pp.

Zucker, F. J., and W. F. Croswell, 2007: Surface-wave antennas. *Antenna Engineering Handbook*, J. L. Volakis, Ed., McGraw-Hill, 10.1–10.27.